

# High-fidelity laser cooling to the quantum ground state of a silicon nanomechanical oscillator

Liu Qiu,<sup>1,\*</sup> Itay Shomroni,<sup>1,\*</sup> Paul Seidler,<sup>2,†</sup> and Tobias J. Kippenberg<sup>1,‡</sup>

<sup>1</sup>*Institute of Physics, École Polytechnique Fédérale de Lausanne, Station 3, CH-1015 Lausanne, Switzerland*

<sup>2</sup>*IBM Research – Zurich, Säumerstrasse 4, CH-8803 Rüschlikon, Switzerland*

(Dated: June 16, 2022)

Silicon optomechanical crystals enable coupling of photonics at telecommunication wavelengths to GHz mechanical modes, giving rise to optomechanical dynamics that can extend well into the resolved-sideband regime. These devices operate in a frequency range compatible with superconducting qubits and could in principle be integrated on the same material platform to create hybrid systems for quantum information applications. Despite these promising characteristics, high-fidelity ground state preparation has to date only been achieved using passive cooling in a dilution refrigerator. Moreover, heating due to optical absorption has limited measurement protocols to short, low-energy optical pulses. Here, we demonstrate continuous-wave laser sideband cooling of an optomechanical system reaching a mean thermal occupancy of  $0.25^{+0.07}_{-0.03}$  quanta, or 80% ground state occupation, verified via motional sideband asymmetry. We achieve this by employing a  $^3\text{He}$  buffer gas environment and employing a device with a high optical quality factor. Our results overcome previous heating limitations and highlight the promise of silicon optomechanical crystals for quantum-enhanced continuous displacement measurements, as low-added-noise optomechanical interfaces for signal transduction and integration with superconducting qubit technology.

Laser cooling techniques developed several decades ago [1–4] have revolutionized many areas of science and technology, with systems ranging from atoms, ions and molecules [5–8] to solid-state structures and macroscopic objects [9–11]. For instance, the capability to initialize phonon modes of trapped ions in their motional ground state underlies some of the most precise quantum logic-based atomic clocks [12] and in general plays a vital role in quantum gates based on trapped ions [13–15]. Among these various systems, engineered on-chip mechanical oscillators play a unique role given their macroscopic nature [16] and their ability to couple to other degrees of freedom. Optomechanical systems, by virtue of coupling the mechanical and electromagnetic degrees of freedom, allow laser cooling of mechanical motion [9, 17–19]. Ground state preparation has been achieved with a range of mechanical systems [20–26]. This has in turn led to realization of various quantum optomechanical phenomena such as preparation of squeezed [27–31] and other nonclassical [32–34] states of mechanical motion, observation of radiation pressure shot noise [35], and measurement of quantum correlations, manifested as ponderomotive squeezing of light [36, 37] or motional sideband asymmetry [17, 38–41]. These successes notwithstanding, the residual thermal occupancy has an impact on a variety of recently emerged applications of optomechanical systems, such as quantum-limited microwave amplifiers utilizing engineered mechanical reservoirs [42], coherent transduction between optical [43] or between microwave and optical fields [44–46], as well as nonreciprocal devices with minimum added noise [47, 48].

Silicon optomechanical crystals [49, 50] that couple an optical mode at telecommunication wavelengths and a localized mechanical mode at GHz frequencies exhibit several exceptional features, including some of the largest vac-

uum coupling rates  $\mathcal{O}(1 \text{ MHz})$  [50] as well as ultra-coherent phonons [51], and have even been used to create optomechanical lattices [52, 53]. Moreover, silicon optomechanical crystals have been employed in a wide range of quantum physics experiments, such as continuous quantum measurements [36, 41, 54], and probabilistic preparation of quantum states [32–34]. More recently, the compatibility of these systems with planar nanofabrication technology and their scalability have motivated studies of optomechanical topological phenomena [53, 55] and coupling to superconducting qubits for quantum information applications [56, 57]. Yet despite these promising features, high-fidelity ground-state preparation of silicon optomechanical crystals has only been possible via passive cooling to milli-Kelvin temperatures in dilution refrigerators [58, 59]. Significant heating due to optical absorption—a consequence of the extremely small optical mode volume and inefficient thermalization [60]—has limited these experiments to ultra-low average photon fluxes, precluding continuous measurements [41, 54, 58] and necessitating pulsed protocols with reduced pulse energy [32–34, 51].

In this work, we demonstrate efficient laser cooling of a silicon optomechanical crystal in the resolved-sideband regime to a mean phonon occupancy of  $0.25^{+0.07}_{-0.03}$  (i.e. 80% ground state occupation), calibrated using motional sideband asymmetry [17, 39, 41, 61, 62]. By employing a  $^3\text{He}$  buffer gas environment, thermalization is improved significantly. In addition, our device exhibits extremely low intrinsic optical absorption and high vacuum optomechanical cooperativity. Our results overcome previous challenges and highlight the great potential of silicon optomechanical crystals for continuous optical quantum-enhanced measurements, such as displacement sensitivity below the standard quantum limit (SQL) [54, 63] and generation of squeezed mechanical states [27–30].

Our experimental system, shown in Fig. 1(a), is similar to that used in previous experiments [41, 50, 54] and consists of a quasi-one-dimensional photonic crystal nanobeam cavity made of silicon. The pattern of holes in the nanobeam results in a cavity in which a confined optical mode is co-localized with

\* These two authors contributed equally.

† pfs@zurich.ibm.com

‡ tobias.kippenberg@epfl.ch

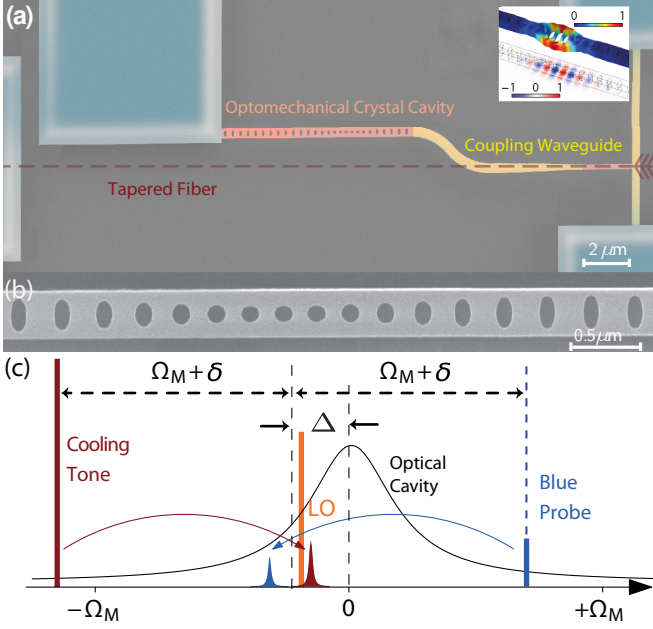


**FIG. 1. Optomechanical crystal and experimental scheme.** (a) False-color SEM image of the silicon optomechanical crystal cavity with a waveguide for input coupling of light. The path of the tapered fiber is indicated by the red dashed line. The inset shows the simulated mechanical breathing mode and optical mode. (b) SEM image of the central portion of the silicon optomechanical crystal cavity. (c) Scheme for motional sideband asymmetry measurement using a cooling tone and a blue probe. The local oscillator (LO) is used for detection and is not sent to the cavity.

a mechanical mode. The optical cavity is single-sided in the sense that the number of holes on the side connected to the coupling waveguide is reduced to create a partially transmitting input mirror. Finite-element simulations of the structure are shown in the inset of Fig. 1(a). A tapered optical fiber is used to couple light evanescently into the coupling waveguide (36% efficiency in this work). A further magnified scanning electron microscopy (SEM) image of the optomechanical crystal cavity is presented in Fig. 1(b). We monitor the laser light reflected from the optical cavity for optomechanical characterization. The optical resonance occurs at  $1540\text{ nm}$  with a total linewidth of  $\kappa/2\pi = 310\text{ MHz}$ , of which the external coupling rate is  $\kappa_{\text{ex}}/2\pi = 120\text{ MHz}$  (the intrinsic linewidth corresponds to a quality factor of  $Q \sim 10^6$ ). The optical mode is coupled to a localized mechanical mode with frequency  $\Omega_m/2\pi = 5.19\text{ GHz}$  and an intrinsic mechanical damping rate of  $\Gamma_{\text{int}}/2\pi = 75\text{ kHz}$ . This places our system deep in the resolved-sideband regime, with a sideband factor  $\Omega_m/\kappa \simeq 17$ . The measured vacuum optomechanical coupling rate is  $g_0/2\pi = 930\text{ kHz}$ .

The optomechanical crystal is mounted in a  $^3\text{He}$  buffer-gas cryostat (Oxford Instruments HelioxTL) capable of cryogenic operation down to  $0.5\text{ K}$ . As detailed in Refs. 41 and 54, the buffer gas environment allows us to overcome the heating due to optical absorption that has otherwise limited operation with such devices to very low photon fluxes [32–34]. Specifically, the gaseous  $^3\text{He}$  ensures more efficient thermalization of the

sample [41]. In this work, we operate the cryostat around  $2.5\text{ K}$  with a buffer gas pressure of  $\sim 20\text{ mbar}$ . The buffer-gas causes additional damping, increasing the mechanical linewidth to  $\Gamma_m = \Gamma_{\text{int}} + \Gamma_{\text{gas}} \simeq 2\pi \times 93\text{ kHz}$ .

Motional sideband asymmetry, a signature of the quantum nature of the optomechanical interaction, was recently observed in optomechanical systems [38–40] and used to perform self-calibrated thermometry of the mechanical oscillator close to its ground state [41, 61, 62]. By measuring the Stokes and anti-Stokes scattered sidebands, proportional to  $\bar{n}_f + 1$  and  $\bar{n}_f$ , respectively, the mean phonon occupancy of the oscillator  $\bar{n}_f$  can be determined. In contrast to previous experiments [61, 62], we adopt a two-tone pumping scheme [Fig. 1(c)]. A strong cooling tone near the lower motional sideband is applied for sideband cooling, while an additional weaker blue probe is applied near the upper motional sideband. The resonantly-enhanced Stokes and anti-Stokes sidebands scattered from the blue probe and cooling tone, respectively, are utilized for sideband thermometry. As shown in Fig. 1(c), the two tones are separated by  $2(\Omega_m + \delta)$ , with  $\delta/2\pi \simeq -40\text{ MHz}$  chosen so that the sidebands do not overlap. The mean of the frequencies of the two pump tones is detuned from the optical resonance by  $\Delta$ . For each sideband asymmetry measurement,  $\Delta$  is inferred by measuring the detuning of the cooling tone from the cavity,  $\Delta_c = \Delta - \Omega_m - \delta$ , using a coherent cavity response measurement [54, 64]. More details on the experimental setup are given in the Supplemental Material.

In the presence of the cooling tone and blue probe, the mechanical susceptibility is modified by the radiation pressure. The effective damping rate of the mechanical oscillator becomes  $\Gamma_{\text{eff}} = \Gamma_m + \Gamma_{\text{opt}}$ , with the total optomechanical damping rate (in the resolved-sideband regime)  $\Gamma_{\text{opt}} = -\Gamma_b + \Gamma_c$ , where

$$\Gamma_{b(c)} = \bar{n}_{b(c)} g_0^2 \left( \frac{\kappa}{\kappa^2/4 + (\Delta \pm \delta)^2} \right), \quad (1)$$

and  $\bar{n}_b$  and  $\bar{n}_c$  are the intracavity photon numbers of the blue probe and cooling tone, respectively. In the weak coupling regime ( $\kappa \gg \Gamma_{\text{opt}}$ ), the effective mechanical frequency is  $\Omega_{\text{eff}} = \Omega_m + \delta\Omega_m$ , with

$$\delta\Omega_m = \bar{n}_b g_0^2 \left( \frac{\Delta + \delta}{\kappa^2/4 + (\Delta + \delta)^2} \right) + \bar{n}_c g_0^2 \left( \frac{\Delta - \delta}{\kappa^2/4 + (\Delta - \delta)^2} \right). \quad (2)$$

The mean final phonon occupancy (in the resolved-sideband regime) is given by

$$\bar{n}_f = \frac{\Gamma_m \bar{n}_{\text{th}} + \Gamma_b}{\Gamma_{\text{eff}}}, \quad (3)$$

where  $\bar{n}_{\text{th}}$  is the mean phonon occupancy due to the thermal environment. We emphasize that the second term in the numerator of Eq. (3) corresponds to quantum backaction (QBA) from the blue probe, which must be taken into account despite the blue probe being weaker, as the motional heating transitions are resonant with the cavity. Indeed, the ratio of QBA

from the blue probe to that from the cooling tone for symmetric pumping at  $\pm\Omega_m$  (i.e.  $\delta/2\pi = \Delta/2\pi = 0$  Hz, and equal power for the two tones) is given by  $16\Omega_m^2/\kappa^2 \approx 4500$ . The heating due to the blue probe is  $\Gamma_b/\Gamma_{\text{eff}}$  and is comparable to the heating by the thermal bath for the highest probe powers, as discussed below. In addition, we note that Eq. (3) is formulated within the rotating-wave approximation, where the QBA due to the cooling tone is negligible [17, 18, 24, 25] as the optomechanical crystal cavity is deeply in the resolved-sideband regime. Further details concerning QBA from the two tones are provided in the Supplemental Material.

To achieve a quantum-limited measurement of the output field, we use balanced heterodyne detection, beating the reflected optical signal with a strong phase-locked local oscillator (LO;  $\sim 6$  mW). The heterodyne signal provides a frequency-shifted spectrum of the mechanical noise. The frequency difference between the LO and the mean frequency of the two pumping tones is  $\Delta_{\text{LO}}$ , where  $0 < \Delta_{\text{LO}} < -\delta$ . The measured heterodyne noise spectrum, normalized to the shot noise floor, is given by

$$S_I(\Omega) = 1 + \eta\Gamma_{\text{eff}} \left[ \frac{(\bar{n}_f + 1)\Gamma_b}{\Gamma_{\text{eff}}^2/4 + (\Omega + \delta - \Delta_{\text{LO}})^2} + \frac{\bar{n}_f\Gamma_c}{\Gamma_{\text{eff}}^2/4 + (\Omega + \delta + \Delta_{\text{LO}})^2} \right], \quad (4)$$

where  $\eta$  is the overall detection efficiency. The second and third terms in Eq. (4) correspond to the scattered Stokes and anti-Stokes sidebands, proportional to  $\bar{n}_f + 1$  and  $\bar{n}_f$ , that we use for self-calibrated thermometry of mechanical motion.

Our scheme differs from previous experiments done in both the microwave [39] and optical [41] domains that utilize equal red and blue probes alongside a cooling tone. By using only two tones, we avoid coupling between scattered thermomechanical sidebands due to Kerr-type nonlinearities that introduce errors in the inferred phonon occupancy [41]. Moreover, the use of weak equal probes becomes impractical at low phonon occupancies, where the signal-to-noise ratio of the anti-Stokes sideband, proportional to  $\bar{n}_f$ , becomes extremely small, and stronger probing would introduce heating from the blue probe. In our approach, the ratio between the input powers of the cooling tone and the blue probe is kept around 9 in all measurements, allowing us to achieve both sufficient sideband cooling and a measurable anti-Stokes signal without undue heating from the blue probe.

In a first set of measurements, we vary the pumping powers of the cooling tone and the blue probe, keeping the power ratio approximately constant and maintaining the relative detuning of the cooling tone with respect to the cavity resonance at  $\Delta_c = -\Omega_m$  for optimal sideband cooling, as shown in Fig 2(a). The value of  $\Delta_c$  is acquired from a coherent cavity response measurement before recording a noise spectrum via balanced heterodyne detection, as detailed in the Supplemental Material. The effective mechanical linewidth  $\Gamma_{\text{eff}}$  as a function of  $\bar{n}_c$  obtained from the noise spectra is presented in Fig. 2(b) (blue dots) with a linear fit (red curve), yielding a mechanical linewidth  $\Gamma_m/2\pi = 93$  kHz and vacuum coupling rate  $g_0/2\pi = 930$  kHz. Figure 2(c) shows a series of measured

noise spectra at various values of  $\bar{n}_c$ , normalized to the shot noise floor, along with Lorentzian fits of the data. The left and right thermomechanical sidebands shown in Fig. 2(c) correspond to the sidebands from the cooling tone and the blue probe, respectively. (Note that the order of the peaks is reversed relative to the actual sideband frequencies because of the relative frequency of the LO.) At very low pumping power (e.g.  $\bar{n}_c = 35$ ), the ratio between red and blue sidebands is  $\sim 6$  due to the difference in power of the two tones as well as the cavity frequency response. As the power increases, this ratio, given by  $\bar{n}_f\Gamma_c/(\bar{n}_f + 1)\Gamma_b$  [cf. Eq. (4)], starts to decrease, as the mechanical oscillator approaches the ground state,  $\bar{n}_f \rightarrow 0$ . At high pumping powers, we also observe an increase in the shot-noise floor due to the large reflected power. Figure 2(d) shows the inferred mean phonon occupancy  $\bar{n}_f$  vs. the cooling-tone intracavity photon number  $\bar{n}_c$ . The phonon occupancy is determined through both sideband asymmetry (green filled circles) and the area under the Lorentzian fit of the cooling tone sideband (purple open circles) in the noise spectrum. The sideband area is calibrated to phonon occupancy by anchoring its value to 2.5 K at the lowest values of  $\bar{n}_c$ . The calculated phonon occupancy follows the theoretical prediction given by Eq. (3) (dashed purple line) but starts to deviate from it at high pumping powers. We attribute this deviation to an increase in thermal bath temperature caused by optical absorption and to an increase in the intrinsic mechanical linewidth [20]. The minimum phonon occupancy of  $0.28_{-0.05}^{+0.12}$  (78% ground-state probability) is reached at high cooling-tone intracavity photon number ( $\bar{n}_c \approx 760$ ).

In a second set of measurements, we vary the detuning of the cooling tone from the cavity resonance  $\Delta_c$ , while keeping the separation of the two tones  $2(\Omega_m + \delta)$ , as well as  $\Delta_{\text{LO}}$ , fixed [cf. Fig. 3(a)]. The input powers are maintained around  $660 \mu\text{W}$  and  $70 \mu\text{W}$  for the cooling tone and the blue probe, respectively. Again, we infer  $\Delta_c$  from the coherent cavity response measurement before recording each noise spectrum via balanced heterodyne detection. Figure 3(b) displays the effective mechanical linewidth (red circles) and the optical spring effect (blue circles) obtained from a multi-Lorentzian fit to the noise spectrum, along with the respective theoretical curves from Eqs. (1) and (2). In the case of the optical spring effect, the value of  $\Delta_c$  appears to be slightly shifted by 40 MHz with respect to the theoretical curve. We attribute this shift mainly to the cavity resonance frequency drift in the time between measurement of the coherent and incoherent optomechanical spectra, as well as to uncertainty in the fit to the coherent response data used to determine  $\Delta_c$ . An error bar of  $\pm 40$  MHz is accordingly assigned to the horizontal axis in Fig. 3(b). Figure 3(c) shows measured noise spectra for various values of  $\Delta_c$  normalized to the shot noise floor and fitted with a multi-Lorentzian function. The left and right thermomechanical peaks in Fig. 3(c) correspond to the sidebands from the cooling tone and the blue probe, respectively, similar to Fig. 2(c). Figure 3(d) (lower panel) shows the integrated thermomechanical noise in the sideband (inferred via the data fitting) for the blue probe and the cooling tone, normalized by each probe input power (without assuming any uncertainty in  $\Delta_c$ ). To infer the mechanical occupancy via side-

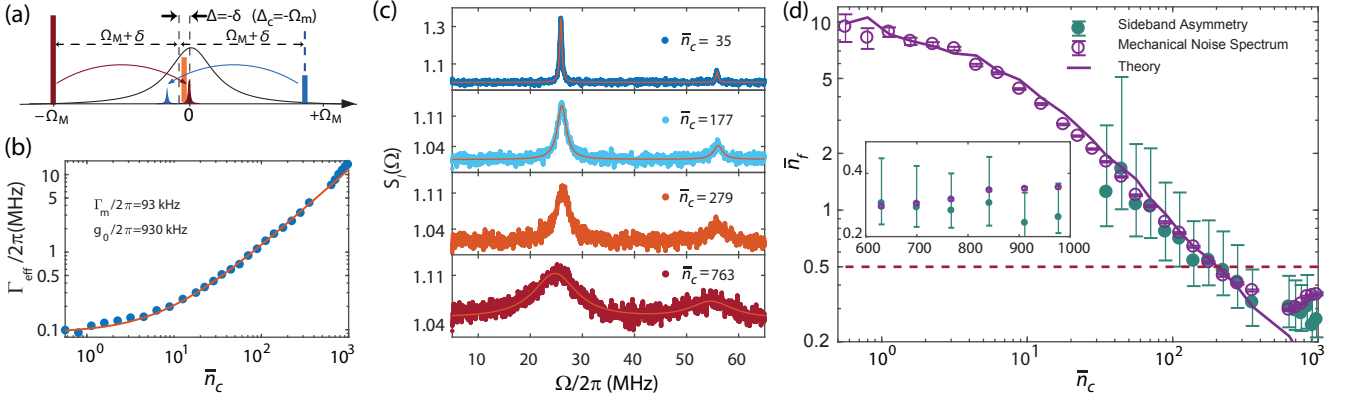


FIG. 2. **Sideband cooling for different cooling tone powers.** (a) Dual tone pumping scheme for the power sweep. The relative detuning to the cavity resonance of cooling tone is maintained as  $-\Omega_m$ , and the frequency separation between the cooling tone and blue probe is fixed at  $2(\Omega_m + \delta)$ . (b) Measured effective mechanical linewidth from the noise power spectral density vs. cooling tone intracavity photon number  $\bar{n}_c$  (blue dots) with a linear fit (red curve), giving mechanical linewidth  $\Gamma_m/2\pi = 93$  kHz and vacuum optomechanical coupling rate  $g_0/2\pi = 930$  kHz. (c) Panels show single-sided noise spectra from balanced heterodyne detection, normalized to the shot noise floor, for different intracavity photon numbers. (d) Mean phonon occupancy vs. intracavity photon number of the cooling tone. The purple empty circles correspond to the calibrated area under the Lorentzian lineshape of the thermomechanical sidebands from the cooling tone, with error bars representing 95% confidence interval on the the area from the Lorentzian fits. The green full circles are inferred from the sideband asymmetry between the thermomechanical sidebands from the blue probe and the cooling tone, where error bars are given by the detuning error of  $\pm 40$  MHz and the Lorentzian fit. The inset shows a zoomed view of the highest cooling powers.

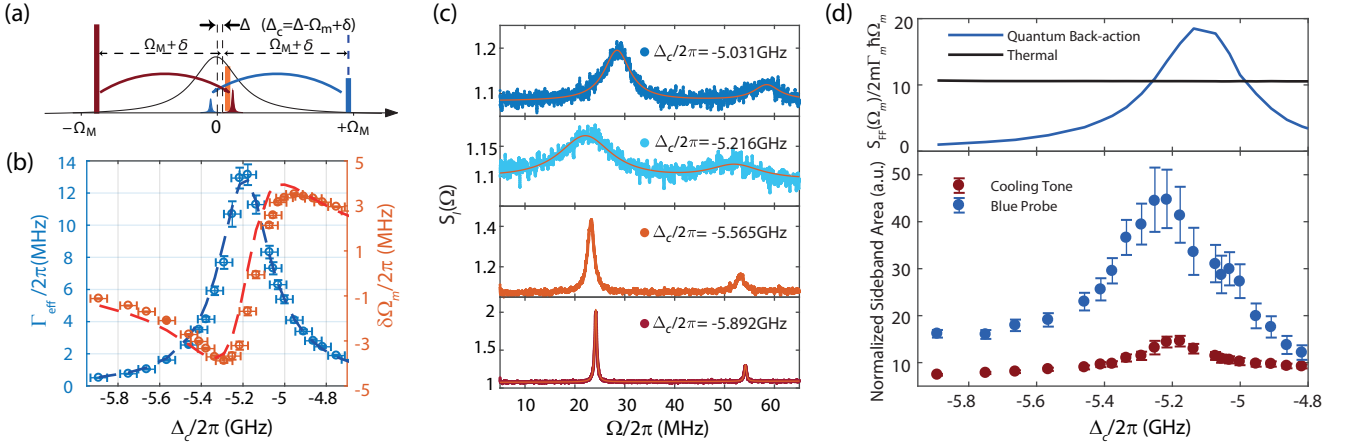


FIG. 3. **Sideband cooling for different detunings of the cooling tone  $\Delta_c$ .** (a) Dual tone pumping scheme for the detuning sweep. The relative detuning to the cavity resonance of cooling tone is swept, while the frequency separation between the cooling tone and blue probe is fixed at  $2(\Omega_m + \delta)$ . (b) The fitted mechanical linewidth (blue circles, left axis) and optical spring effect (red circles, right axis), with corresponding theoretical plots (dashed lines) based on experimental parameters. The horizontal error bars are due to the detuning uncertainty of  $\pm 40$  MHz and vertical error bars are from the fitting of the noise spectrum. (c) Panels show single-sided noise spectra from the balanced heterodyne detection, normalized to the shot noise floor, for different detunings. (d) The lower panel shows the sideband areas normalized by the input power, for the blue probe (blue dots) and the cooling tone (red dots). The error bars correspond to the fitting error of the noise spectrum. The upper panel shows the force spectral density at positive mechanical frequency  $S_{FF}(+\Omega_m)$  for both the thermal force (black curve) and the QBA from the blue probe (blue curve) with experimental parameters, normalized by  $2m\Gamma_m\hbar\Omega_m$ .

band thermometry, the detuning-dependent intracavity photon number and the optical susceptibility for the two scattered sidebands must also be taken into consideration, as detailed in the Supplemental Material. These corrections, necessary when using a detuning sweep of two tones, lead to the presence of a sideband asymmetry in the power-normalized data even for the low cooling rates when the cooling tone is far from the lower sideband [e.g., near  $\Delta_c/2\pi = -5.9$  GHz in

Fig. 3 (c)]. Importantly, these corrections vanish in the case of  $\Delta_c = -\Omega_m - \delta$ , i.e. when  $\Delta/2\pi = 0$  Hz. Hence, the large difference in the normalized sideband areas of the two tones around  $\Delta_c/2\pi = -5.2$  GHz in Fig. 3(d) indicates the very low mechanical occupancy  $\bar{n}_f$ . We note that, for optimal sideband cooling, it is required that  $\Delta_c = -\Omega_m$ . Optical heating via absorption of photons from the two tones would lead to an increase in sideband area that is weakly dependent on detuning



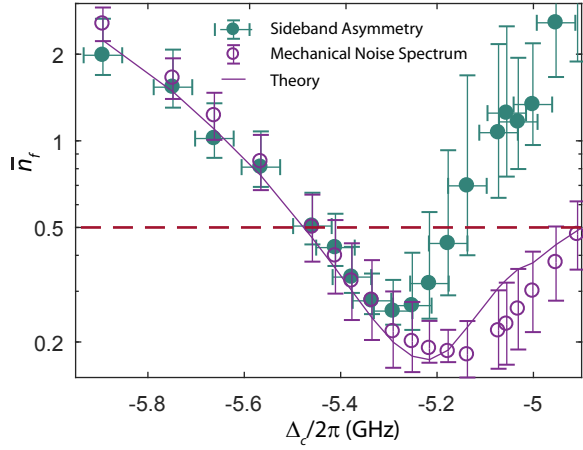


FIG. 4. **Calibrated phonon occupancy  $\bar{n}_f$  vs. the detuning of the cooling tone  $\Delta_c$ .** The data show  $\bar{n}_f$  calibrated from sideband asymmetry (green full circles) and cooling tone sideband area (purple empty circles) with a theory curve (purple) with experimental parameters. In the sideband asymmetry calibration, the horizontal error bars correspond to detuning uncertainty of  $\pm 40$  MHz while vertical error bars include both fitting error of the noise spectrum and the detuning uncertainty. In the cooling tone sideband area calibration, the error bars correspond to the fitting error of the noise spectrum.

for  $\Delta_c$  near  $-\Omega_m$  (i.e. due to the tail of the cavity Lorentzian far off-resonance). In contrast, the QBA associated with the blue probe is strongly detuning-dependent and is expected to lead to an increased sideband area around  $\Delta_c = -\Omega_m - 2\delta$  as shown in Eq. (1). The force noise spectral density at the positive mechanical frequency  $S_{FF}(+\Omega_m)$  (responsible for heating the mechanical oscillator [65]) of the QBA from the blue probe and of the thermal force noise, as calculated from experimental parameters, are displayed in the upper panel of Fig. 3(d). Here, we express  $S_{FF}(+\Omega_m)$  in mechanical quanta via normalization by  $2m\Gamma_m\hbar\Omega_m$ , where  $m$  is the effective mass. While the thermal force spectral density is independent of detuning (equivalent to  $\bar{n}_{th} \sim 10$  quanta), the force spectral density due to QBA from the blue probe (equivalent to  $\Gamma_b/\Gamma_m$ ) peaks around  $\Delta_c/2\pi = -5.1$  GHz, where it dominates the thermal force noise. Weak evidence of this QBA heating by the blue probe can be seen in Fig. 3(d) (lower panel) as a shoulder at  $\Delta_c/2\pi \simeq -5.1$  GHz in the data for the blue probe sideband area.

Figure 4 shows  $\bar{n}_f$  vs.  $\Delta_c$  calibrated from the sideband asymmetry and cooling tone sideband area as green filled circles and purple open circles, respectively. The theoretical dependence calculated from experimental parameters (3) is shown as a purple curve for comparison. The theory curve matches quite well over the entire range of  $\Delta_c$  to the values of  $\bar{n}_f$  determined from the cooling-tone sideband area. There is also good agreement between  $\bar{n}_f$  determined from the sideband asymmetry and that from the cooling-tone sideband area for cooling-tone detuning on the red side of the mechanical sideband (i.e.  $\Delta_c/2\pi < -5.3$  GHz). However, the data from the sideband asymmetry measurement deviates from theory for  $\Delta_c/2\pi > -5.2$  GHz. The deviation may have several dif-

ferent causes. The detuning uncertainty of  $\Delta_c$  is assigned to error bars in both horizontal and vertical axis for the sideband asymmetry calibration. In addition, the ratio of the blue-probe sideband area to that of the cooling tone becomes very small (e.g.  $< 0.15$ ) when  $\Delta_c/2\pi > -4.9$  GHz, due to the detuning-dependent difference in intracavity photon number between the two tones, as detailed in the Supplemental Material. This makes the sideband asymmetry calibration more vulnerable to systematic drifts and potential uncertainties in the noise measurement. We note however that the deviation cannot be a result of classical noise in the pumping tones. As is evident from Fig. 4,  $\bar{n}_f$  determined from the sideband asymmetry is larger than that determined from cooling-tone sideband area. If excess laser noise were present, noise squashing of the cooling-tone sideband and anti-squashing of the blue-probe sideband would lead to lower values of  $\bar{n}_f$  calculated from sideband asymmetry. The minimum phonon occupancy, occurring close to the red mechanical sideband ( $\Delta_c/2\pi \simeq -5.29$  GHz) is  $\bar{n}_f = 0.25^{+0.07}_{-0.03}$ , placing the mechanical oscillator deep into the ground state with 80% ground state occupation. Note that we have taken the more conservative value for the minimum  $\bar{n}_f$ , namely that given by sideband asymmetry, rather than the even lower value given by the cooling-tone sideband area. As can be seen from Eq. (3), the final occupancy of the sideband-cooled mechanical oscillator is limited to  $\Gamma_b/\Gamma_{eff}$  by QBA from the blue probe in the two-tone pumping scheme used here. Here, this corresponds to a limiting phonon occupancy of 0.13 at optimal detuning ( $\Delta_c = -\Omega_m$ ). The estimated residual phonon occupancy due to optical absorption heating is  $\sim 0.06$ , much lower than in previous experiments [54].

In conclusion, we demonstrated high-fidelity sideband cooling of a localized GHz mechanical mode of a silicon optomechanical crystal to a mean phonon occupancy of  $0.25^{+0.07}_{-0.03}$  (80% ground state occupation). Importantly, our analysis shows that optical absorption heating plays a minor role in our sample. This puts the system in a unique position, combining high mechanical frequency, large sideband resolution, operation close to the ground state and the ability to achieve strong probing. These characteristics open the door to a large number of quantum optomechanical experiments that have remained elusive in the optical domain, including two-tone backaction-evading measurements reaching sub-SQL sensitivity [54, 66, 67], reservoir-engineered squeezed mechanical states [27–30, 68], non-reciprocal devices with low added noise [47, 48], as well as quantum-coherent operations such as state swapping [69] and entanglement generation [70].

## ACKNOWLEDGMENTS

LQ acknowledges support by the Swiss National Science Foundation under grant No. 163387. IS acknowledges support by the European Union's Horizon 2020 research and innovation programme under Marie Skłodowska-Curie IF grant agreement No. 709147 (GeNoSOS). This work is supported by the Swiss National Science Foundation under grant No. 163387 and grant No. 51NF40-160591 (NCCR-QSIT), and the European Unions Horizon 2020 research and innovation programme under grant

No. 732894 (FET Proactive HOT). Samples were fabricated in the Binnig and Rohrer Nanotechnology Center at IBM Research – Zurich and at the Center of MicroNanoTechnology (CMI) at EPFL.

## DATA AVAILABILITY STATEMENT

All data and analysis files will be made available via [zenodo.org](https://zenodo.org) upon publication.

- 
- [1] S. Chu, *Reviews of Modern Physics* **70**, 685 (1998).
  - [2] C. N. Cohen-Tannoudji, *Reviews of Modern Physics* **70**, 707 (1998).
  - [3] C. E. Wieman, D. E. Pritchard, and D. J. Wineland, *Reviews of Modern Physics* **71**, S253 (1999).
  - [4] T. J. Kippenberg and K. J. Vahala, *Science* **321**, 1172 (2008), [arXiv:0712.1618](https://arxiv.org/abs/0712.1618).
  - [5] A. Ashkin, *Physical Review Letters* **40**, 729 (1978).
  - [6] D. J. Wineland and W. M. Itano, *Physical Review A* **20**, 1521 (1979), [arXiv:arXiv:1011.1669v3](https://arxiv.org/abs/1011.1669v3).
  - [7] E. S. Shuman, J. F. Barry, and D. Demille, *Nature* **467**, 820 (2010), [arXiv:1103.6004](https://arxiv.org/abs/1103.6004).
  - [8] L. Anderegg, B. L. Augenbraun, Y. Bao, S. Burchesky, L. W. Cheuk, W. Ketterle, and J. M. Doyle, *Nature Physics* **14**, 890 (2018), [arXiv:1803.04571](https://arxiv.org/abs/1803.04571).
  - [9] A. Schliesser, P. Del’Haye, N. Nooshi, K. J. Vahala, and T. J. Kippenberg, *Physical Review Letters* **97**, 243905 (2006), [arXiv:0611235 \[physics\]](https://arxiv.org/abs/0611235).
  - [10] T. Li, S. Kheifets, and M. G. Raizen, *Nature Physics* **7**, 527 (2011), [arXiv:1101.1283](https://arxiv.org/abs/1101.1283).
  - [11] LIGO Scientific Collaboration, *New Journal of Physics* **11**, 73032 (2009).
  - [12] P. O. Schmidt, T. Rosenband, C. Langer, W. M. Itano, J. C. Bergquist, and D. J. Wineland, *Science* **309**, 749 (2005).
  - [13] C. Ospelkaus, U. Warring, Y. Colombe, K. R. Brown, J. M. Amini, D. Leibfried, and D. J. Wineland, *Nature* **476**, 181 (2011), [arXiv:1104.3573](https://arxiv.org/abs/1104.3573).
  - [14] C. Monroe and J. Kim, *Science* **339**, 1164 (2013), [arXiv:0402594v3 \[arXiv:cond-mat\]](https://arxiv.org/abs/0402594v3).
  - [15] R. Blatt and C. F. Roos, *Nature Physics* **8**, 277 (2012), [arXiv:0905.0118](https://arxiv.org/abs/0905.0118).
  - [16] M. Aspelmeyer, T. J. Kippenberg, and F. Marquardt, *Reviews of Modern Physics* **86**, 1391 (2014), [arXiv:1303.0733](https://arxiv.org/abs/1303.0733).
  - [17] I. Wilson-Rae, N. Nooshi, W. Zwerger, and T. J. Kippenberg, *Physical Review Letters* **99**, 093901 (2007), [arXiv:0702113 \[cond-mat\]](https://arxiv.org/abs/0702113).
  - [18] F. Marquardt, J. P. Chen, A. A. Clerk, and S. M. Girvin, *Physical Review Letters* **99**, 093902 (2007), [arXiv:0701416 \[cond-mat\]](https://arxiv.org/abs/0701416).
  - [19] A. Schliesser, R. Rivière, G. Anetsberger, O. Arcizet, and T. J. Kippenberg, *Nature Physics* **4**, 415 (2008), [arXiv:0709.4036](https://arxiv.org/abs/0709.4036).
  - [20] J. Chan, T. P. Alegre, A. H. Safavi-Naeini, J. T. Hill, A. Krause, S. Gröblacher, M. Aspelmeyer, and O. Painter, *Nature* **478**, 89 (2011), [arXiv:1106.3614](https://arxiv.org/abs/1106.3614).
  - [21] J. D. Teufel, T. Donner, D. Li, J. W. Harlow, M. S. Allman, K. Cicak, A. J. Sirois, J. D. Whittaker, K. W. Lehnert, and R. W. Simmonds, *Nature* **475**, 359 (2011), [arXiv:1103.2144](https://arxiv.org/abs/1103.2144).
  - [22] E. Verhagen, S. Deléglise, S. Weis, A. Schliesser, and T. J. Kippenberg, *Nature* **482**, 63 (2012), [arXiv:1107.3761](https://arxiv.org/abs/1107.3761).
  - [23] D. J. Wilson, V. Sudhir, N. Piro, R. Schilling, A. Ghadimi, and T. J. Kippenberg, *Nature* **524**, 325 (2015), [arXiv:1410.6191](https://arxiv.org/abs/1410.6191).
  - [24] R. W. Peterson, T. P. Purdy, N. S. Kampel, R. W. Andrews, P. L. Yu, K. W. Lehnert, and C. A. Regal, *Physical Review Letters* **116**, 1 (2016), [arXiv:1510.03911](https://arxiv.org/abs/1510.03911).
  - [25] J. B. Clark, F. Lecocq, R. W. Simmonds, J. Aumentado, and J. D. Teufel, *Nature* **541**, 191 (2017), [arXiv:1606.08795](https://arxiv.org/abs/1606.08795).
  - [26] M. Rossi, D. Mason, J. Chen, Y. Tsaturyan, and A. Schliesser, *Nature* **563**, 53 (2018), [arXiv:1805.05087](https://arxiv.org/abs/1805.05087).
  - [27] A. Kronwald, F. Marquardt, and A. A. Clerk, *Physical Review A* **88**, 063833 (2013), [arXiv:1307.5309](https://arxiv.org/abs/1307.5309).
  - [28] F. Lecocq, J. B. Clark, R. W. Simmonds, J. Aumentado, and J. D. Teufel, *Physical Review X* **5**, 041037 (2015), [arXiv:1509.01629](https://arxiv.org/abs/1509.01629).
  - [29] E. E. Wollman, C. U. Lei, A. J. Weinstein, J. Suh, A. Kronwald, F. Marquardt, A. A. Clerk, and K. C. Schwab, *Science* **349**, 952 (2015), [arXiv:1507.01662](https://arxiv.org/abs/1507.01662).
  - [30] J. M. Pirkkalainen, E. Damskägg, M. Brandt, F. Massel, and M. A. Sillanpää, *Physical Review Letters* **115**, 243601 (2015), [arXiv:1507.04209](https://arxiv.org/abs/1507.04209).
  - [31] C. F. Ockeloen-Korppi, E. Damskägg, J. M. Pirkkalainen, M. Asjad, A. A. Clerk, F. Massel, M. J. Woolley, and M. A. Sillanpää, *Nature* **556**, 478 (2018), [arXiv:1711.01640](https://arxiv.org/abs/1711.01640).
  - [32] R. Riedinger, S. Hong, R. A. Norte, J. A. Slater, J. Shang, A. G. Krause, V. Anant, M. Aspelmeyer, and S. Gröblacher, *Nature* **530**, 313 (2016), [arXiv:1512.05360](https://arxiv.org/abs/1512.05360).
  - [33] S. Hong, R. Riedinger, I. Marinković, A. Wallucks, S. G. Hofer, R. A. Norte, M. Aspelmeyer, and S. Gröblacher, *Science* **358**, 203 (2017), [arXiv:1706.03777](https://arxiv.org/abs/1706.03777).
  - [34] I. Marinković, A. Wallucks, R. Riedinger, S. Hong, M. Aspelmeyer, and S. Gröblacher, *Phys. Rev. Lett.* **121**, 220404 (2018).
  - [35] T. P. Purdy, R. W. Peterson, and C. A. Regal, *Science* **339**, 801 (2013), [arXiv:1209.6334](https://arxiv.org/abs/1209.6334).
  - [36] A. H. Safavi-Naeini, S. Gröblacher, J. T. Hill, J. Chan, M. Aspelmeyer, and O. Painter, *Nature* **500**, 185 (2013), [arXiv:1302.6179](https://arxiv.org/abs/1302.6179).
  - [37] T. P. Purdy, P.-L. Yu, R. W. Peterson, N. S. Kampel, and C. A. Regal, *Physical Review X* **3**, 031012 (2013), [arXiv:1306.1268](https://arxiv.org/abs/1306.1268).
  - [38] A. H. Safavi-Naeini, J. Chan, J. T. Hill, T. P. M. Alegre, A. Krause, and O. Painter, *Physical Review Letters* **108**, 033602 (2012), [arXiv:1108.4680](https://arxiv.org/abs/1108.4680).
  - [39] A. J. Weinstein, C. U. Lei, E. E. Wollman, J. Suh, A. Metelmann, A. A. Clerk, and K. C. Schwab, *Physical Review X* **4**, 041003 (2014), [arXiv:1404.3242](https://arxiv.org/abs/1404.3242).
  - [40] V. Sudhir, D. J. Wilson, R. Schilling, H. Schütz, S. A. Fedorov, A. H. Ghadimi, A. Nunnenkamp, and T. J. Kippenberg, *Physical Review X* **7**, 011001 (2017), [arXiv:1602.05942](https://arxiv.org/abs/1602.05942).

- [41] L. Qiu, I. Shomroni, M. A. Ioannou, D. Malz, A. Nunnenkamp, and T. Kippenberg, **2018-July**, **1** (2018), [arXiv:1805.12364](#).
- [42] L. D. Toth, N. R. Bernier, A. Nunnenkamp, A. K. Feofanov, and T. J. Kippenberg, *Nature Physics* **13**, 787 (2017), [arXiv:1602.05180](#).
- [43] J. T. Hill, A. H. Safavi-Naeini, J. Chan, and O. Painter, *Nature Communications* **3**, 1196 (2012), [arXiv:1206.0704](#).
- [44] J. Bochmann, A. Vainsencher, D. D. Awschalom, and A. N. Cleland, *Nature Physics* **9**, 712 (2013).
- [45] R. W. Andrews, R. W. Peterson, T. P. Purdy, K. Cicak, R. W. Simmonds, C. A. Regal, and K. W. Lehnert, *Nature Physics* **10**, 321 (2014), [arXiv:1310.5276](#).
- [46] A. P. Higginbotham, P. S. Burns, M. D. Urmey, R. W. Peterson, N. S. Kampel, B. M. Brubaker, G. Smith, K. W. Lehnert, and C. A. Regal, *Nature Physics* **14**, 1038 (2018), [arXiv:1712.06535](#).
- [47] G. A. Peterson, F. Lecocq, K. Cicak, R. W. Simmonds, J. Aumentado, and J. D. Teufel, *Physical Review X* **7**, 031001 (2017), [arXiv:1703.05269](#).
- [48] N. R. Bernier, L. D. Tóth, A. Koottandavida, M. A. Ioannou, D. Malz, A. Nunnenkamp, A. K. Feofanov, and T. J. Kippenberg, *Nature Communications* **8**, 604 (2017).
- [49] M. Eichenfield, J. Chan, R. M. Camacho, K. J. Vahala, and O. Painter, *Nature* **462**, 78 (2009), [arXiv:0906.1236](#).
- [50] J. Chan, A. H. Safavi-Naeini, J. T. Hill, S. Meenehan, and O. Painter, *Applied Physics Letters* **101**, 081115 (2012), [arXiv:1206.2099](#).
- [51] G. S. MacCabe, H. Ren, J. Luo, J. D. Cohen, H. Zhou, A. Sipahigil, M. Mirhosseini, and O. Painter, (2019), [arXiv:1901.04129](#).
- [52] K. Fang, M. H. Matheny, X. Luan, and O. Painter, *Nature Photonics* **10**, 489 (2016), [arXiv:1508.05138](#).
- [53] M. Schmidt, S. Kessler, V. Peano, O. Painter, and F. Marquardt, *Optica* **2**, 635 (2015).
- [54] I. Shomroni, L. Qiu, D. Malz, A. Nunnenkamp, and T. J. Kippenberg, (2018), [10.1002/jps.10412](#), [arXiv:1809.01007](#).
- [55] C. Brendel, V. Peano, O. J. Painter, and F. Marquardt, *Proceedings of the National Academy of Sciences* **114**, 3390 (2017).
- [56] A. J. Keller, P. B. Dieterle, M. Fang, B. Berger, J. M. Fink, and O. Painter, *Applied Physics Letters* **111**, 042603 (2017), [arXiv:1703.10195](#).
- [57] P. Arrangoiz-Arriola, E. A. Wollack, M. Pechal, J. D. Witmer, J. T. Hill, and A. H. Safavi-Naeini, *Physical Review X* **8**, 031007 (2018), [arXiv:1804.03625](#).
- [58] S. M. Meenehan, J. D. Cohen, S. Gröblacher, J. T. Hill, A. H. Safavi-Naeini, M. Aspelmeyer, and O. Painter, *Physical Review A* **90**, 011803 (2014), [arXiv:1403.3703](#).
- [59] S. M. Meenehan, J. D. Cohen, G. S. MacCabe, F. Marsili, M. D. Shaw, and O. Painter, *Physical Review X* **5** (2015), [10.1103/PhysRevX.5.041002](#), [arXiv:1503.05135](#).
- [60] M. G. Holland, *Physical Review* **132**, 2461 (1963).
- [61] T. P. Purdy, P.-L. Yu, N. S. Kampel, R. W. Peterson, K. Cicak, R. W. Simmonds, and C. A. Regal, *Physical Review A* **92**, 031802 (2015), [arXiv:arXiv:1406.7247v1](#).
- [62] M. Underwood, D. Mason, D. Lee, H. Xu, L. Jiang, A. B. Shkarin, K. Børkje, S. M. Girvin, and J. G. E. Harris, *Physical Review A* **92**, 061801 (2015), [arXiv:1406.7254](#).
- [63] D. Mason, J. Chen, M. Rossi, Y. Tsaturyan, and A. Schliesser, , **1** (2018), [arXiv:1809.10629](#).
- [64] A. H. Safavi-Naeini, T. P. Alegre, J. Chan, M. Eichenfield, M. Winger, Q. Lin, J. T. Hill, D. E. Chang, and O. Painter, *Nature* **472**, 69 (2011), [arXiv:1012.1934](#).
- [65] A. A. Clerk, M. H. Devoret, S. M. Girvin, F. Marquardt, and R. J. Schoelkopf, *Reviews of Modern Physics* **82**, 1155 (2010), [arXiv:0810.4729](#).
- [66] J. Suh, A. J. Weinstein, C. U. Lei, E. E. Wollman, S. K. Steinke, P. Meystre, A. A. Clerk, and K. C. Schwab, *Science* **344**, 1262 (2014).
- [67] I. Shomroni, A. Youssefi, N. Sauerwein, L. Qiu, P. Seidler, D. Malz, A. Nunnenkamp, and T. J. Kippenberg, , **1** (2018), [arXiv:1812.11022](#).
- [68] C. Lei, A. Weinstein, J. Suh, E. Wollman, A. Kronwald, F. Marquardt, A. Clerk, and K. Schwab, *Physical Review Letters* **117**, 100801 (2016).
- [69] T. A. Palomaki, J. W. Harlow, J. D. Teufel, R. W. Simmonds, and K. W. Lehnert, *Nature* **495**, 210 (2013).
- [70] T. A. Palomaki, J. D. Teufel, R. W. Simmonds, and K. W. Lehnert, *Science* **342**, 710 (2013).
- [71] A. J. Weinstein, *Quantum Electromechanics with Two Tone Drive*, *phd*, California Institute of Technology (2016).
- [72] S. Weis, R. Rivière, S. Deléglise, E. Gavartin, O. Arcizet, A. Schliesser, and T. J. Kippenberg, *Science* **330**, 1520 (2010), [arXiv:1007.0565](#).

# High-fidelity laser cooling to the quantum ground state of a silicon nanomechanical oscillator

## Supplemental Material

Liu Qiu,<sup>1,\*</sup> Itay Shomroni,<sup>1,\*</sup> Paul Seidler,<sup>2,†</sup> and Tobias J. Kippenberg<sup>1,‡</sup>

<sup>1</sup>*Institute of Physics, École Polytechnique Fédérale de Lausanne, Lausanne CH-1015, Switzerland*

<sup>2</sup>*IBM Research – Zurich, Säumerstrasse 4, CH-8803 Rüschlikon, Switzerland*

<sup>†</sup>Electronic address: pfs@zurich.ibm.com

<sup>‡</sup>Electronic address: tobias.kippenberg@epfl.ch

(Dated: June 16, 2022)

### I. THEORY

In our experiment, we pump the optomechanical system with two tones, one close to the red mechanical sideband and the other close to the blue mechanical sideband of the cavity. The amplitude of the input field takes the form  $a_{\text{in}} = a_c e^{-i\omega_c t} + a_b e^{-i\omega_b t} + \delta a_{\text{in}}$ , where  $a_{c(b)}$  and  $\omega_{c(b)}$  are the amplitude and frequency for the cooling tone (blue probe), and  $\delta a_{\text{in}}$  corresponds to the input noise. The two tones are separated by  $2(\Omega_m + \delta)$ , and the mean of their frequencies is detuned from the cavity resonance by  $\Delta$ , as shown in Fig. 1 in the main text. The mechanical mode is coupled to the optical field through radiation pressure and is additionally coupled to a thermal reservoir. By linearizing the intracavity optical field  $a$  to  $\bar{a} + \delta a$  and the mechanical displacement field  $b$  to  $\bar{b} + \delta b$ , we obtain the quantum Langevin equations for the fluctuation of the intracavity fields in the frame rotating at the mean of the frequencies of the blue probe and the cooling tone [16, 29, 39]. Within the rotating-wave approximation,

$$\begin{aligned}\delta \dot{a} &= \left(i\Delta - \frac{\kappa}{2}\right)\delta a + i(g_c \delta b + g_b \delta b^\dagger) + \sqrt{\kappa_{\text{ex}}}\delta a_{\text{in}} + \sqrt{\kappa_0}\delta a_{\text{vac}} \\ \delta \dot{b} &= \left(i\delta - \frac{\Gamma_m}{2}\right)\delta b + i(g_c \delta a + g_b \delta a^\dagger) + \sqrt{\Gamma_m}\delta b_{\text{in}},\end{aligned}\quad (\text{S1})$$

where  $g_b = \sqrt{\bar{n}_b}g_0$  and  $g_c = \sqrt{\bar{n}_c}g_0$ .  $\bar{n}_{b(c)}$  is the intracavity photon number for the blue probe (cooling tone) and  $g_0$  is the vacuum optomechanical coupling rate.  $\kappa$ ,  $\kappa_0$  and  $\kappa_{\text{ex}}$  are the total, intrinsic and external optical loss rates of the optical

mode.  $\Gamma_m$  is the mechanical damping rate.  $\delta a_{\text{in}}$ ,  $\delta a_{\text{vac}}$  and  $\delta b_{\text{in}}$  correspond to the optical input noise, optical vacuum noise and the mechanical noise. The optical and mechanical noise operators satisfy the following noise correlations,

$$\begin{aligned}\langle \delta a_{\text{in}}(t) \delta a_{\text{in}}^\dagger(t') \rangle &= \alpha \delta(t - t') \\ \langle \delta a_{\text{in}}^\dagger(t) \delta a_{\text{in}}(t') \rangle &= 0 \\ \langle \delta a_{\text{vac}}(t) \delta a_{\text{vac}}^\dagger(t') \rangle &= \alpha \delta(t - t') \\ \langle \delta a_{\text{vac}}^\dagger(t) \delta a_{\text{vac}}(t') \rangle &= 0 \\ \langle \delta b_{\text{in}}(t) \delta b_{\text{in}}^\dagger(t') \rangle &= \bar{n}_{\text{th}} \delta(t - t') \\ \langle \delta b_{\text{in}}^\dagger(t) \delta b_{\text{in}}(t') \rangle &= (\bar{n}_{\text{th}} + \beta) \delta(t - t'),\end{aligned}\quad (\text{S2})$$

where  $\bar{n}_{\text{th}} = k_B T / \hbar \Omega_m$  is the mean phonon occupation of the mechanical oscillator in equilibrium with the thermal reservoir at temperature  $T$ . Here  $\alpha$  describes the fluctuation in the optical field while  $\beta$  describes the zero-point fluctuation in the mechanical motion. In general,  $\alpha$  (for a quantum limited laser) and  $\beta$  equal to one.

Here we define the optical and mechanical susceptibility as

$$\begin{aligned}\chi_c(\omega) &:= \frac{1}{\kappa/2 - i(\omega + \Delta)} \\ \chi_m(\omega) &:= \frac{1}{\Gamma_m/2 - i(\omega + \delta)}.\end{aligned}$$

Solving Eq. (S1) in the Fourier domain, we thus obtain

$$\begin{aligned}\delta a &= \chi_c(\omega)(\sqrt{\kappa_{\text{ex}}}\delta a_{\text{in}}(\omega) + \sqrt{\kappa_0}\delta a_{\text{vac}}(\omega) + i g_c \delta b + i g_b \delta b^\dagger) \\ \delta a^\dagger &= \chi_c^*(-\omega)(\sqrt{\kappa_{\text{ex}}}\delta a_{\text{in}}^\dagger(\omega) + \sqrt{\kappa_0}\delta a_{\text{vac}}^\dagger(\omega) - i g_c \delta b^\dagger - i g_b \delta b) \\ \begin{pmatrix} \delta b(\omega) \\ \delta b^\dagger(\omega) \end{pmatrix} &= \frac{i\sqrt{\kappa_{\text{ex}}}}{N(\omega)} \begin{pmatrix} \chi_c(\omega)g_c(\chi_m^{*-1}(-\omega) + G^2\chi_c^*(-\omega)) & \chi_c^*(-\omega)g_b(\chi_m^{*-1}(-\omega) + G^2\chi_c(\omega)) \\ \chi_c(\omega)g_b(\chi_m^{-1}(\omega) + G^2\chi_c^*(-\omega)) & \chi_c^*(-\omega)g_c(\chi_m^{-1}(\omega) + G^2\chi_c(\omega)) \end{pmatrix} \begin{pmatrix} \delta a_{\text{in}} \\ \delta a_{\text{in}}^\dagger \end{pmatrix} \\ &\quad + \frac{i\sqrt{\kappa_0}}{N(\omega)} \begin{pmatrix} \chi_c(\omega)g_c(\chi_m^{*-1}(-\omega) + G^2\chi_c^*(-\omega)) & \chi_c^*(-\omega)g_b(\chi_m^{*-1}(-\omega) + G^2\chi_c(\omega)) \\ \chi_c(\omega)g_b(\chi_m^{-1}(\omega) + G^2\chi_c^*(-\omega)) & \chi_c^*(-\omega)g_c(\chi_m^{-1}(\omega) + G^2\chi_c(\omega)) \end{pmatrix} \begin{pmatrix} \delta a_{\text{vac}} \\ \delta a_{\text{vac}}^\dagger \end{pmatrix} \\ &\quad + \frac{\sqrt{\Gamma_m}}{N(\omega)} \begin{pmatrix} \chi_m^{*-1}(-\omega) - i\Sigma^*(-\omega) & -i\Pi(\omega) \\ i\Pi(\omega) & \chi_m^{-1}(\omega) + i\Sigma(\omega) \end{pmatrix} \begin{pmatrix} \delta b_{\text{in}} \\ \delta b_{\text{in}}^\dagger \end{pmatrix},\end{aligned}\quad (\text{S3})$$

where

$$N(\omega) = \chi_m^{-1}(\omega)\chi_m^{*-1}(-\omega) + i\chi_m^{*-1}(-\omega)\Sigma(\omega) - i\chi_m^{-1}(\omega)\Sigma^*(-\omega) + G^4\chi_c(\omega)\chi_c^*(-\omega) \quad (\text{S4})$$



and

$$\Pi(\omega) = -ig_c g_b [\chi_c(\omega) - \chi_c^*(-\omega)] \quad (\text{S5})$$

$$\Sigma(\omega) = -i[g_c^2 \chi_c(\omega) - g_b^2 \chi_c^*(-\omega)] \quad (\text{S6})$$

$$G^2 = g_c^2 - g_b^2. \quad (\text{S7})$$

The mechanical susceptibility, which is modified by the radiation pressure from the two tones, is defined as

$$\begin{aligned} \chi_{\text{meff}}(\omega) &= \frac{\chi_m^*(-\omega) - i\Sigma^*(-\omega)}{N(\omega)} \\ &\approx \frac{1}{(\Gamma_m + \Gamma_{\text{opt}})/2 - i(\omega + \delta - \delta\Omega_m)}. \end{aligned} \quad (\text{S8})$$

During the measurements, the ratio of cooling-tone to blue-probe pumping powers is fixed around 9. In the weak-coupling regime ( $\kappa \gg \Gamma_{\text{opt}}$ ), the effective damping rate of the mechanical oscillator becomes  $\Gamma_{\text{eff}} = \Gamma_m + \Gamma_{\text{opt}}$ , where the optomechanical damping rate (in the resolved-sideband limit) is  $\Gamma_{\text{opt}} = -\Gamma_b + \Gamma_c$ , and  $\Gamma_b$  and  $\Gamma_c$  take the form

$$\Gamma_{b(c)} = \bar{n}_{b(c)} g_0^2 \left( \frac{\kappa}{\kappa^2/4 + (\Delta \pm \delta)^2} \right). \quad (\text{S9})$$

The optical spring effect is given by

$$\begin{aligned} \delta\Omega_m &= \bar{n}_b g_0^2 \left( \frac{\Delta + \delta}{\kappa^2/4 + (\Delta + \delta)^2} \right) \\ &\quad + \bar{n}_c g_0^2 \left( \frac{\Delta - \delta}{\kappa^2/4 + (\Delta - \delta)^2} \right). \end{aligned} \quad (\text{S10})$$

From the Wiener-Khinchin theorem, the two-sided mechanical displacement noise spectrum is calculated in the lab frame as

$$\begin{aligned} \frac{S_{xx}(\omega)}{x_{\text{zpf}}^2} &= S_{bb}(\omega) + S_{b^\dagger b^\dagger}(\omega) \\ &= \frac{\Gamma_m (\bar{n}_{\text{th}} + 1) + \Gamma_c}{(\omega - \Omega_{\text{eff}})^2 + \Gamma_{\text{eff}}^2/4} \\ &\quad + \frac{\Gamma_m \bar{n}_{\text{th}} + \Gamma_b}{(\omega + \Omega_{\text{eff}})^2 + \Gamma_{\text{eff}}^2/4}. \end{aligned} \quad (\text{S11})$$

The final mechanical occupation, in the sideband resolved limit, is given by

$$\bar{n}_f = \frac{\Gamma_m \bar{n}_{\text{th}} + \Gamma_b}{\Gamma_{\text{eff}}}. \quad (\text{S12})$$

In the two-tone pumping scheme, the quantum backaction (QBA) from the blue probe can become dominant even when there is no heating due to optical absorption, as is evident from the second term in the numerator of Eq. (S12).

When coupled to both the optical and thermal reservoir, the zero point fluctuation of the dressed mechanical mode [71], becomes

$$\tilde{\beta} = \frac{\alpha(\Gamma_c - \Gamma_b) + \Gamma_m \beta}{\Gamma_{\text{eff}}}. \quad (\text{S13})$$

For  $\alpha = 1$  (i.e. a quantum limited laser field) and  $\beta = 1$ , we see that also  $\tilde{\beta} = 1$ .

We note that Eq. (S12) is formulated using the rotating-wave approximation, where the QBA from the cooling tone is negligible [17, 18, 25], as the system is deep in the resolved-sideband regime. In the following, we explain this conclusion using a Raman-scattering picture that addresses QBA from both the cooling tone and the blue probe [18]. Without the mechanical damping, the mean phonon occupancy of the optomechanical crystal cavity  $\bar{n}_{\text{min}}$  is given by the detailed balance expression

$$\frac{\bar{n}_{\text{min}} + 1}{\bar{n}_{\text{min}}} = \frac{\Gamma_b^{AS} + \Gamma_c^{AS}}{\Gamma_b^S + \Gamma_c^S}, \quad (\text{S14})$$

where  $\Gamma_{b(c)}^{AS}$  and  $\Gamma_{b(c)}^S$  correspond to the anti-Stokes and Stokes scattering rate, respectively, of the blue probe (cooling tone). Now,  $\Gamma_c^{AS} = \Gamma_c$  and  $\Gamma_b^S = \Gamma_b$ , whereas  $\Gamma_b^{AS}$  and  $\Gamma_c^S$  take the form

$$\begin{aligned} \Gamma_b^{AS} &= \bar{n}_b g_0^2 \left( \frac{\kappa}{\kappa^2/4 + (\Delta + \delta + 2\Omega_m)^2} \right) \\ \Gamma_c^S &= \bar{n}_c g_0^2 \left( \frac{\kappa}{\kappa^2/4 + (\Delta - \delta - 2\Omega_m)^2} \right). \end{aligned} \quad (\text{S15})$$

The imbalanced Stokes and anti-Stokes scattering from both the cooling tone and the blue probe leads to a net optomechanical damping of the mechanical oscillator  $\Gamma_{\text{opt}} = \Gamma_b^{AS} + \Gamma_c^{AS} - \Gamma_b^S - \Gamma_c^S \approx \Gamma_c - \Gamma_b$ . The minimum phonon occupancy  $\bar{n}_{\text{min}}$  is therefore given by

$$\bar{n}_{\text{min}} = \frac{\Gamma_c^S + \Gamma_b}{\Gamma_{\text{opt}}}. \quad (\text{S16})$$

The stochastic QBA force from both tones produces a residual phonon occupancy of the optomechanical crystal cavity. In the deep-resolved-sideband regime ( $\kappa \ll \Omega_m$ ), such that  $\Gamma_c^S \ll \Gamma_{\text{opt}}$ , the QBA from the cooling tone is negligible. After including the mechanical damping  $\Gamma_m$ ,  $\bar{n}_f$  takes the form in Eq. (S12), where the QBA from only the blue probe is considered.

Adopting the standard input-output formalism, we can obtain the output optical field  $\delta a_{\text{out}} = \delta a_{\text{in}} - \sqrt{\kappa_{\text{ex}}} \delta a$ . To achieve a quantum-limited measurement of the output field, we use balanced heterodyne detection, beating the reflected optical signal with a strong local oscillator ( $\sim 6$  mW). The frequency difference between the local oscillator and the mean frequency of the two pumping tones is  $\Delta_{\text{LO}}$ , where  $0 < \Delta_{\text{LO}} < -\delta$ . This places the local oscillator in between the thermomechanical sidebands from the two pumping tones, which is necessary because of the limited bandwidth of the balanced heterodyne detectors. The measured single-sided heterodyne noise spectrum corresponds to the symmetrized autocorrelator of the photocurrent,  $S_I(\Omega) = \frac{1}{2} \int_{-\infty}^{\infty} \langle \{\hat{I}_{\text{out}}(t + t'), \hat{I}_{\text{out}}(t')\} \rangle e^{i\Omega t} dt$ , and, when normalized to the shot noise, is given by

$$\begin{aligned} S_I(\Omega) &= 1 + \eta \Gamma_{\text{eff}} \left[ \frac{(\bar{n}_f + 1) \Gamma_b}{\Gamma_{\text{eff}}^2/4 + (\Omega + \delta - \Delta_{\text{LO}})^2} \right. \\ &\quad \left. + \frac{\bar{n}_f \Gamma_c}{\Gamma_{\text{eff}}^2/4 + (\Omega + \delta + \Delta_{\text{LO}})^2} \right], \end{aligned} \quad (\text{S17})$$

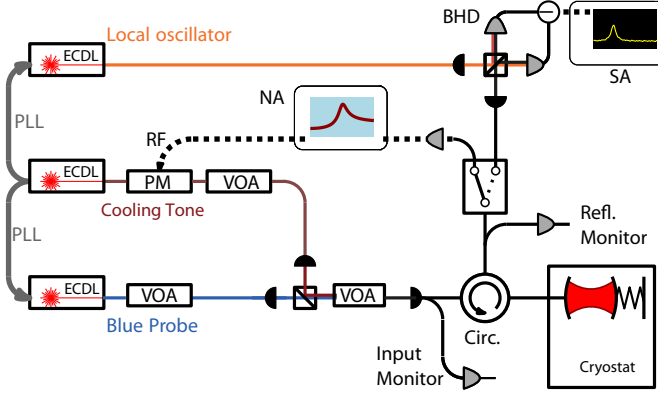


FIG. S1. **Experimental setup.** ECDL, external-cavity diode laser; PM, phase modulator; VOA, variable optical attenuator; BHD, balanced heterodyne detector; SA, spectrum analyzer; NA, network analyzer; PLL, phase-locked loop.

where  $\eta$  is the overall detection efficiency. In (S17), the first term corresponds of course to the shot noise, whereas the second and third terms correspond to the thermomechanical sidebands of the blue probe and cooling tone, which are located at  $-\delta + \Delta_{LO}$  and  $-\delta - \Delta_{LO}$ , respectively. In the main text, Eq. (S17) is utilized to determine the phonon occupancy from the asymmetry of the motional sidebands.

## II. FABRICATION

Our optomechanical crystal cavities are fabricated on a silicon-on-insulator wafer (Soitec) with a top-silicon device-layer thickness of 220 nm and a buried-oxide layer thickness of 2  $\mu\text{m}$ . We pattern our chips by electron beam lithography using 4% hydrogen silsesquioxane (HSQ) as a negative resist. Pattern transfer into the device layer is accomplished by inductively-coupled-plasma reactive ion etching (ICP-RIE) with a mixture of HBr and  $\text{O}_2$ . To permit input/output coupling with a tapered fiber, an additional photolithography step is performed followed by reactive ion etching (RIE) with a mixture of  $\text{SF}_6$  and  $\text{C}_4\text{F}_8$  to create a mesa structure. After resist removal, the buried oxide layer is partially removed in 10% hydrofluoric acid to create free-standing devices. Following a Piranha (a mixture of sulfuric acid and hydrogen peroxide) cleaning step to remove organic residues, the sample is finally dipped into 2% hydrofluoric acid to terminate the silicon surface with hydrogen atoms. The chip is then immediately mounted on the sample holder for characterization and loaded into the cryostat.

## III. EXPERIMENTAL SYSTEM DETAILS

The experiments are performed in a  $^3\text{He}$  buffer gas cryostat (Oxford Instruments HelioxTL) capable of reaching a base temperature of 500 mK. The surrounding gaseous  $^3\text{He}$  improves the thermalization of the silicon optomechanical crystal cavity and thereby significantly diminishes the temperature increase

due to optical absorption, as shown in previous optomechanical experiments [41, 54]. In our experiment, we chose to work at 2.5 K with the  $^3\text{He}$  buffer gas pressure around 20 mbar.

A schematic of the experimental setup is shown in Fig. S1. Three external cavity diode lasers (ECDLs) generate the local oscillator, cooling tone, and blue probe. The blue probe and the local oscillator (LO) are phase-locked to the cooling tone. The cooling tone passes through a phase modulator (PM) that can be used to generate weak sidebands as probes for coherent optomechanical spectroscopy. The cooling tone and the blue probe are combined in free-space with the same polarization and sent into a single-mode fiber that enters the cryostat. The single-pass coupling efficiency from the tapered fiber to the cavity input mirror is  $\sim 36\%$ . A fiber-optic circulator feeds the reflected light to the detection stage, which can be toggled between two different paths. In the first path, the reflected light impinges on a fast photoreceiver and the RF signal is sent to a network analyzer for coherent optomechanical spectroscopy, in which case the phase modulator is employed. In the second path, the reflected light is sent to a balanced heterodyne detection (BHD) setup, where it is mixed with a strong local oscillator ( $\sim 6$  mW) on balanced photodetectors. The power spectral density of the photocurrent is analyzed by a spectrum analyzer. In this case, the cooling tone is not phase modulated.

## IV. DATA ANALYSIS

A single measurement consists of acquisition of the power spectral density for given system parameters (cooling tone power, detuning, etc.) and determination of the phonon occupancy according to Eq. (S17). This requires reliable characterizations of  $\kappa$ ,  $\bar{n}_c$ ,  $\bar{n}_b$  and  $\Delta_c$ . A measurement proceeds as follows. First, we determine the individual powers of the cooling tone and blue probe (both input and reflected) by blocking each in turn. We nominally set the blue probe power to be a factor of 9 weaker than the cooling tone. Second, we perform coherent optomechanical spectroscopy to determine  $\Delta_c$  and  $\kappa$ . Third, we switch to the BHD setup and acquire the power spectral density of the photocurrent. Fourth, we record again the total input and reflected probe powers. The probe powers fluctuate by less than 1% across measurements.

We note that excess laser noise is also known to constrain sideband cooling and to corrupt motional sideband asymmetry measurements. As shown in previous work [41], the excess laser noise at a frequency of 5.2 GHz at typical probing powers is negligible compared to quantum fluctuation of the light.

Figure S2 shows typical coherent optomechanical spectra at several different values of  $\Delta_c$ , with the same fixed input powers for the cooling tone and the blue probe as in Fig. 3 in the main text. The mechanical motion leads to destructive interference with the probe generated by the phase modulator, resulting in optomechanically induced transparency (OMIT) [64, 72] in the reflected cavity response. We fit the data with a theoretical model described by Ref. 64 (black lines) to extract  $\kappa$  and  $\Delta_c$ , which are also used, along with the measured powers, to determine  $\bar{n}_b$  and  $\bar{n}_c$ .

A typical incoherent noise spectrum from the balanced het-

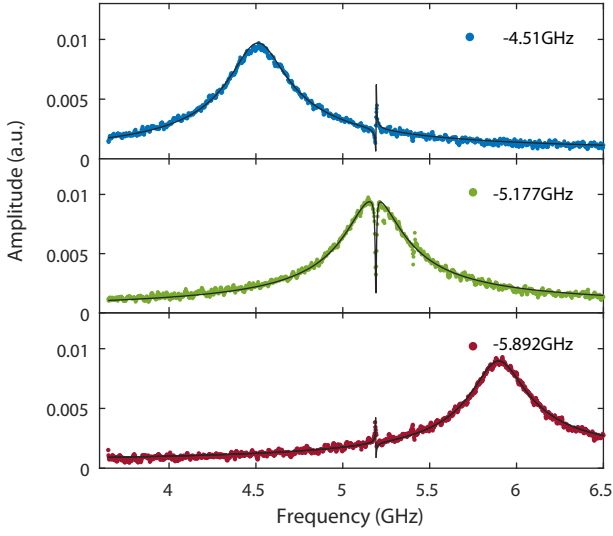


FIG. S2. **Coherent optomechanical spectroscopy.** The three panels show various detunings of the cooling tone with respect to the optical resonance, with fixed input powers for the cooling tone ( $\sim 660 \mu\text{W}$ ) and the blue probe ( $\sim 70 \mu\text{W}$ ). The optomechanically-induced transparency in the reflected cavity response is fitted with a theoretical model (black curve).

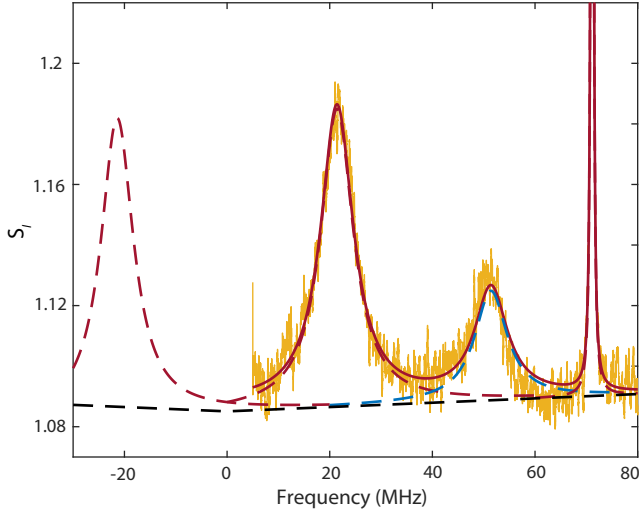


FIG. S3. **Fitting of the incoherent noise spectrum.** Typical noise spectrum (orange) with  $\Delta_c/2\pi \simeq -5.29 \text{ GHz}$  fitted with a sum of Lorentzians (red solid curve; see Eq. S18). The individual Lorentzian components are indicated by dashed curves. Note that part of the tail of the anti-Stokes sideband (red dashed) is folded over zero frequency when mixed with the local oscillator. This tail is taken into account in the fit by including an additional, negative frequency Lorentzian. The blue dashed Lorentzian is the Stokes sideband. The narrow peak (clipped) is the Stokes sideband from another, weakly-coupled mechanical mode. The black dashed curve corresponds to the noise floor.

erodyne detection is shown in Fig. S3 (orange). The single-sided spectrum consists of the Stokes and anti-Stokes scattered sidebands. Importantly, the tail of the anti-Stokes sideband is folded over from negative frequencies and needs to be taken into account when performing the fit. In addition, an anti-Stokes sideband from another nearby mechanical mode is present above 70 MHz. We accordingly use a fitting function with five Lorentzian terms,

$$S_{\text{fit}}(\omega) = c + \frac{a_1}{1 + 4(\omega - \omega_1)^2/\Gamma_{\text{eff}}^2} + \frac{a_1}{1 + 4(\omega + \omega_1)^2/\Gamma_{\text{eff}}^2} + \frac{a_2}{1 + 4(\omega - \omega_2)^2/\Gamma_{\text{eff}}^2} + \frac{a_2}{1 + 4(\omega + \omega_2)^2/\Gamma_{\text{eff}}^2} + \frac{a_3}{1 + 4(\omega - \omega_3)^2/\Gamma_{\text{eff}}^2}, \quad (\text{S18})$$

where  $c$ ,  $a_1$ ,  $a_2$ ,  $a_3$ ,  $\omega_1$ ,  $\omega_2$ ,  $\omega_3$ ,  $\Gamma_{\text{eff}}$ , and  $\Gamma'_{\text{eff}}$  are the fitting parameters.  $c$  corresponds to the noise background.  $a_1$  ( $a_2$ ) and  $\omega_1$  ( $\omega_2$ ) correspond to the amplitude and central frequency of the sideband from the cooling tone (blue probe) for the mechanical mode of interest, with effective linewidth  $\Gamma_{\text{eff}}$ . The second and third terms in Eq. (S18) correspond to the anti-Stokes sideband and its negative counterpart (dashed red in Fig. S3), and similarly for the fourth and fifth terms and the Stokes sideband (dashed blue; only positive frequency shown). The last term in Eq. (S18) takes into account anti-Stokes scattering from the second mechanical mode at  $\Omega'_m/2\pi \simeq 5.24 \text{ GHz}$  with mechanical damping rate  $\Gamma'_{\text{eff}}$ . The optomechanical coupling for this mode is much weaker, resulting in an optomechanically broadened linewidth below  $2\pi \times 1 \text{ MHz}$ . In Fig. S3, the noise floor is indicated by the black dashed curve, where we include a linear increase over the entire 70 MHz frequency span. We note that the increase is negligible ( $< 0.5\%$ ), even for the highest pumping power.

The integrated area under the thermomechanical sidebands from the cooling tone and the blue probe are given by  $A_1 = a_1\Gamma_{\text{eff}}/4$  and  $A_2 = a_2\Gamma_{\text{eff}}/4$ , respectively, and are proportional to  $\Gamma_c\bar{n}_f$  and  $\Gamma_b(\bar{n}_f + 1)$ . The phonon occupancy was calibrated from the noise spectrum in two different ways. In the power-sweep series, where  $\Delta_c = -\Omega_m$ , the mean phonon occupancy of the mechanical oscillator is  $\bar{n}_{\text{th}} = k_B T / \hbar \Omega_m$ , if the mechanical mode is in equilibrium with the thermal reservoir, which we assume is the case for low  $\bar{n}_c$  (e.g.  $\bar{n}_c^0 < 1$ ). The mean phonon occupancy  $\bar{n}_f$  at higher  $\bar{n}_c$  is then inferred by comparing the integrated area of the noise spectrum of the anti-Stokes sideband  $A_1$  to the area at low power  $A_1^0$ :

$$\bar{n}_f = \frac{A_1 \bar{n}_c^0 k_B T}{A_1^0 \bar{n}_c \hbar \Omega_m}. \quad (\text{S19})$$

Alternatively, sideband asymmetry between the Stokes and anti-Stokes sidebands can be used to determine the mean phonon occupancy,

$$\bar{n}_f = \frac{A_2 \Gamma_b}{A_1 \Gamma_c - A_2 \Gamma_b}, \quad (\text{S20})$$

where  $\Gamma_b$  and  $\Gamma_c$  are given by Eq. (S9).

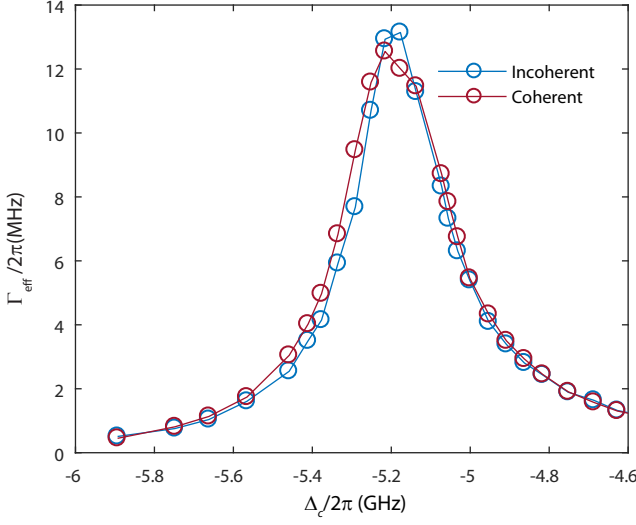


FIG. S4. **Comparison of effective linewidth obtained from coherent and incoherent measurements.** Data show effective mechanical linewidth  $\Gamma_{\text{eff}}$  obtained from coherent optomechanical spectroscopy (red) and incoherent heterodyne detection (blue) versus detuning of the cooling tone.

## V. ERROR ANALYSIS

As noted earlier, before and after each set of measurements, both the input powers and the reflected powers of the two tones are checked, and their fluctuation is less than 1%. For the mean phonon occupancy calibration, the largest uncertainty is therefore  $\Delta_c$ , the relative detuning of the pumping tones with respect to the cavity. As discussed in the main text, measurement of the optical spring effect reveals an offset of 40 MHz in  $\Delta_c$  [Fig. 3(b)]. There may be several reasons for the offset, such as a shift in the cavity frequency due to temperature drift in the time between the coherent and incoherent optomechanical spectroscopy measurements or an intracavity-photon-dependent mechanical linewidth and frequency change [20]. Figure S4 shows the fitted effective mechanical linewidth  $\Gamma_{\text{eff}}$  from both the incoherent (blue) and coherent (red) optomechanical spectroscopy in the detuning series. There is a small drift in the  $\Delta_c$  ( $\sim 2\pi \times 40$  MHz) between the two sets of data. We therefore adopt a detuning uncertainty of  $\pm 40$  MHz for  $\Delta_c$  in both the power-sweep and the detuning-sweep series of measurements. This is greater than the fitting error of  $\pm 10$  MHz in  $\Delta_c$  obtained from the coherent optomechanical spectra.

Figure S5(a) shows the ratio of the optical susceptibility for the sideband from the blue probe to the optical susceptibility for the sideband from the cooling tone versus  $\Delta_c$ ,

$$R = \frac{(\kappa/2)^2 + (\Delta_c + \Omega_m)^2}{(\kappa/2)^2 + (\Delta_c + \Omega_m + 2\delta)^2}. \quad (\text{S21})$$

The gray area illustrates the uncertainty in  $R$  resulting from the  $\pm 40$  MHz uncertainty in  $\Delta_c$ . The detuning uncertainty is taken into consideration for the sideband thermometry and

is included in the error bars in Figs. 2(d) and 4 in the main text, in addition to the Lorentzian fitting error from the noise

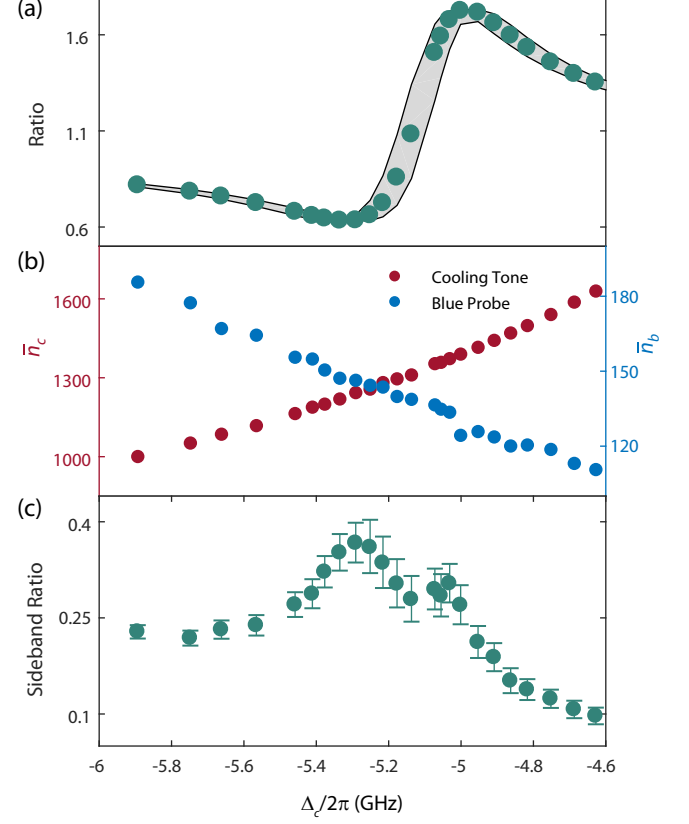


FIG. S5. **Data analysis for the detuning-sweep series.** (a) Ratio of the optical susceptibilities for the sidebands from the blue probe and the cooling tone versus the detuning of the cooling tone  $\Delta_c$ . The gray area corresponds to the uncertainty in the ratio considering detuning uncertainty of  $\pm 40$  MHz. (b) Intracavity photon number for the cooling tone (red) and the blue probe (blue). (c) Raw ratio of blue-probe to cooling-tone sideband area. See text for details. Error bars correspond to the fitting error of the noise spectrum.

spectrum. Figure S5(c) presents the Stokes-to-anti-Stokes ratio of sideband area, inferred from the fit to the raw data (i.e., without correcting for differences in power or optical susceptibility, see Fig. 3(c) in the main text). This is in contrast to the lower panel of Fig. 3(d) in the main text, where the areas have been normalized to the input power. The ratio reaches a maximum around the red mechanical sideband,  $\Delta_c \simeq -\Omega_m$ . Due to the detuning-dependent variation in intracavity photon number for the two tones (see Fig. S5(b)), the ratio of sideband areas is much larger for large red detunings, i.e. when  $\Delta_c/2\pi < -5.5$  GHz, than for  $\Delta_c/2\pi > -4.9$  GHz. In the latter case, the small ratio, resulting from the large blue detuning of the weak blue probe, makes the asymmetry measurement much more vulnerable to systematic drift and uncertainty. This may account for the large deviation of the phonon occupancy determined by sideband asymmetry from that determined by cooling tone sideband area, as depicted in Fig. 4 in the main text.